

Electromagnon in ferrimagnetic ε -Fe₂O₃ nanograin ceramics

Christelle Kadlec,¹ Filip Kadlec,^{1,*} Veronica Goian,¹ Martí Gich,² Martin Kempa,¹ Stéphane Rols,³ Maxim Savinov,¹ Jan Prokleška,⁴ Milan Orlita,⁵ and Stanislav Kamba¹

¹*Institute of Physics, Academy of Sciences of the Czech Republic,
Na Slovance 2, 182 21 Prague 8, Czech Republic*

²*Institut de Ciència de Materials de Barcelona—Consejo Superior de Investigaciones Científicas,
Campus UAB, 08193, Bellaterra, Catalunya, Spain*

³*Institut Laue-Langevin, BP 156, 38042 Grenoble Cedex 9, France*

⁴*Faculty of Mathematics and Physics, Department of Condensed Matter Physics,
Charles University, Ke Karlovu 5, 121 16 Prague 2, Czech Republic*

⁵*Grenoble High Magnetic Field Lab, CNRS - 25, avenue des Martyrs, Grenoble Cedex 9, France*

Electromagnons are known from multiferroics as spin waves excited by the electric component of electromagnetic radiation. We report the discovery of an excitation in the far-infrared spectra of ε -Fe₂O₃ which we attribute to an electromagnon appearing below 110 K, where the ferrimagnetic structure becomes incommensurately modulated. Inelastic neutron scattering shows that the electromagnon energy corresponds to that of a magnon from the Brillouin zone boundary. Dielectric measurements did not reveal any sign of ferroelectricity in ε -Fe₂O₃ down to 10 K, despite its acentric crystal structure. This shows that the activation of an electromagnon requires, in addition to the polar ferrimagnetic structure, a modulation of the magnetic structure. We demonstrate that a combination of inelastic neutron scattering with infrared and / or terahertz spectroscopies allows detecting electromagnons in ceramics, where no crystal-orientation analysis of THz and infrared spectra is possible.

PACS numbers: 76.50.+g, 77.22.-d, 63.20.kd, 75.85.+t

I. INTRODUCTION

In the last years, there has been an increasing interest in so-called multiferroic materials, displaying simultaneously spontaneous ferroelectric (FE) polarization and ferro- or antiferromagnetic (AFM) ordering. Multiferroics exhibit a rich variety of fundamental physical phenomena, and it is generally believed that they have a potential for novel applications in non-volatile memories^{1,2}, magnonics³ and magnetic sensors⁴. These applications would rely on the coupling of order parameters on various time scales, from quasi-static to ultrafast. However, the understanding of the microscopic mechanism of the magnetodielectric coupling is still a fundamental problem of solid state physics. The static and dynamic magnetoelectric (ME) couplings can have different origins. Owing to the static ME coupling, the macroscopic FE polarization emerges in the cycloidal or transverse conical modulated magnetic structures; this polarization can change with magnetic field. In contrast, the dynamic ME coupling generates an oscillatory polarization and leads to a dielectric dispersion in the terahertz (THz) region. Indeed, THz studies of multiferroics revealed a new kind of electric-field-active spin excitations contributing to the dielectric permittivity $\varepsilon = \varepsilon' - i\varepsilon''$, called electromagnons (EMs)⁵. Their characteristic feature is a coupling with polar phonons, which manifests itself in the spectra by a transfer of dielectric strength from phonons to EMs on cooling⁶. In contrast to ferromagnetic and AFM resonances, which are magnons from the Brillouin zone (BZ) center contributing to the magnetic permeability $\mu = \mu' - i\mu''$, the EMs can be activated also outside

of the BZ center^{7–10}. The understanding of this fact is not trivial, because the photons which excite EMs have wavevectors much smaller than the EMs. Thus, to date, there are several different theories attempting to explain the observed properties of EMs in various materials^{7,9–11}.

The EMs were discovered first in TbMnO₃ and GdMnO₃⁵ which belong to multiferroics denoted¹¹ as type II, where the FE order is induced by a special magnetic ordering. Since then, EMs were confirmed in numerous type-II multiferroics^{6,7,12–18}. Other reports of EMs in type-I multiferroics (e.g. BiFeO₃^{19–21} or hex-YMnO₃²²) appear inconclusive, since no transfer of the dielectric strength from polar phonons to EMs was observed^{19,22}. Also, recent infrared IR and THz studies did not confirm the EM in hex-YMnO₃²³.

Here we report experiments which reveal an excitation identified as an EM in the ferrimagnetic ε phase of Fe₂O₃. Thanks to its chemical simplicity, this phase appears also as a suitable model system for theoretical studies of electromagnonic excitations. While ε -Fe₂O₃ is quite rare and less known than the α (hematite) or γ (maghemite) phases of ε -Fe₂O₃²⁴, its properties make it attractive for applications, such as electromagnetic-wave absorbers and memories^{25–27}. Owing to limited phase stability, it can be synthesized only in the form of nanoparticles tens of nanometers in size^{26,28}, epitaxial thin films²⁹ or nanowires a few micrometers long³⁰. Below 480–495 K, it is ferrimagnetic^{31,32}; at room-temperature, it has a collinear spin structure³³ and exhibits a coercive field of $H_c \approx 2$ T³¹—the highest known value among metal oxides. The crystal lattice has a temperature-independent non-centrosymmetric orthorhombic structure with the

$Pna2_1$ space group³⁴ (magnetic space group $Pn'a2'_1$). It consists of three crystallographically non-equivalent FeO_6 octahedra, forming chains along the a direction, and one type of FeO_4 tetrahedra^{28,35}. Compared to isostructural GaFeO_3 , the low-temperature phase diagram of $\varepsilon\text{-Fe}_2\text{O}_3$ is complex—below 150 K, a series of magnetic phase transitions occurs. Below $T_m = 110$ K, an incommensurate magnetic ordering appears where the magnetic structure modulation has a periodicity of about 10 unit cells³⁵. Near T_m , a drop in ε' was observed, and magnetocapacitive measurements revealed a quadratic coupling³⁶. Room-temperature microwave measurements provided evidence of a strong ferromagnetic resonance (FMR) near 0.74 meV (frequency of 180 GHz) which can be tuned by doping with Al, Ga or Rh^{25–27}. In order to gain insight into the dynamic ME properties of $\varepsilon\text{-Fe}_2\text{O}_3$, we obtained THz, IR and inelastic neutron scattering (INS) spectra of $\varepsilon\text{-Fe}_2\text{O}_3$ nano-grain ceramics upon cooling down to 10 K, providing information about polar and magnetic excitations.

II. SAMPLES AND EXPERIMENTAL METHODS

The nanoparticles of $\varepsilon\text{-Fe}_2\text{O}_3$ were synthesized by sol-gel chemistry. $\text{SiO}_2\text{-Fe}_2\text{O}_3$ composite gels containing 30 wt. % of Fe_2O_3 were prepared from iron nitrate non-hydrate (Sigma-Aldrich > 98%) and tetraethoxysilane (TEOS, Sigma-Aldrich 98%) in hydroethanolic medium at $\text{TEOS:H}_2\text{O:EtOH} = 1:6:6$ molar ratio. Iron nitrate was first dissolved and then TEOS added dropwise to the mixture under stirring. The sol was poured into 5 cm diameter petri dishes that were closed with its cover and gelation took place for between 4 and 5 weeks. The gels were dried overnight in a stove at 70 °C, crushed and thermally treated in air atmosphere for 3 hours at 1100 °C (heating rate 80 °C/h). The resulting material was a composite of $\varepsilon\text{-Fe}_2\text{O}_3$ nanoparticles of about 25 nm in diameter dispersed in an amorphous SiO_2 matrix as checked by X-ray diffraction (XRD) which did not reveal any trace of other Fe_2O_3 polymorphs. The silica was removed by stirring the composite powder for 12 h in a 12M aqueous NaOH solution at 80 °C under reflux. XRD patterns recorded after the silica removal revealed that the microstructure and the phase stability of $\varepsilon\text{-Fe}_2\text{O}_3$ nanoparticles were not affected by the etching process. The nanoparticles were further processed by spark plasma sintering (SPS) in order to prepare a pellet suitable for dielectric, terahertz (THz) and IR measurements by pressing the $\varepsilon\text{-Fe}_2\text{O}_3$ powder in a graphite mould for 4 minutes at 350 °C under 100 MPa. The XRD analysis of the sintered pellet showed that the SPS process did not induce any grain growth or phase transformation. Finally, the SPS pellets were polished to thin disks with a thickness of 1.2 mm. Some IR and THz measurements were performed on $\varepsilon\text{-Fe}_2\text{O}_3$ pellets with a diameter of about 6 mm, which were prepared from powder

at room temperature using a standard tabletop manual hydraulic press (Perkin Elmer). The spectra were qualitatively the same, only the value of the high-frequency IR reflectance was affected by the roughness of the sample surface, which could not be polished.

IR reflectance measurements with the resolution of 0.25 meV were performed using the Fourier transform infrared spectrometer Bruker IFS-113v in near-normal reflectance geometry with an incidence angle of 11°. An Oxford Instruments Optistat optical cryostat with polyethylene windows was used for sample cooling down to 10 K, and a liquid-He-cooled Si bolometer operating at 1.6 K was applied as a detector. We also measured far-IR reflectivity with applied magnetic field up to 13 T. To this aim, another Bruker IFS-113v spectrometer and a custom-made superconducting magnetic cryostat allowing the measurements at 2 and 4 K were used. Time-domain THz spectroscopy was based on measurements of sample transmittance using custom-made spectrometers based on Ti:sapphire femtosecond lasers; one with an Optistat cryostat with mylar windows for measurements without magnetic field but with a higher frequency resolution, enabling to discern the FMR profile, and one with an Oxford Instruments Spectromag cryostat, enabling measurements with magnetic field of up to 7 T. Here, the Voigt configuration was used with the external static magnetic field B_{ext} perpendicular to the magnetic component of the THz radiation B_{THz} . Similar effects were observed also for $B_{\text{ext}} \parallel B_{\text{THz}}$.

INS experiments were performed between 10 and 190 K using about 3 g of loose $\varepsilon\text{-Fe}_2\text{O}_3$ nanopowder in the IN4 time-of-flight diffractometer at the Institut Laue-Langevin in Grenoble, France.

III. RESULTS AND DISCUSSION

A. Broad-band study of the electromagnetic response.

Fig. 1a shows the far and mid-IR reflectivity spectra displaying polar optical phonons of $\varepsilon\text{-Fe}_2\text{O}_3$ between 10 and 300 K. Figs. 1b, c show the far-IR $\varepsilon(E)$ spectra calculated from the fits of IR reflectivity together with the experimental THz data. To this purpose, we used a model involving 35 harmonic oscillators; this number is lower than the number of IR active modes provided by the factor group analysis (see Appendix A); apparently, a part of the modes are too weak to be observed. Upon cooling, all phonons above 12 meV exhibit the usual behavior—their intensity increases due to reduced phonon damping at low temperatures. The TO1 phonon near 11 meV exhibits an anomalous behavior: on cooling, its intensity increases only down to 115 K. Below this temperature, it markedly weakens, while a supplementary broad reflectivity peak develops below $E \sim 10$ meV and becomes more intense upon cooling (see the inset of Fig. 1a). This transfer of strengths involves also the TO2

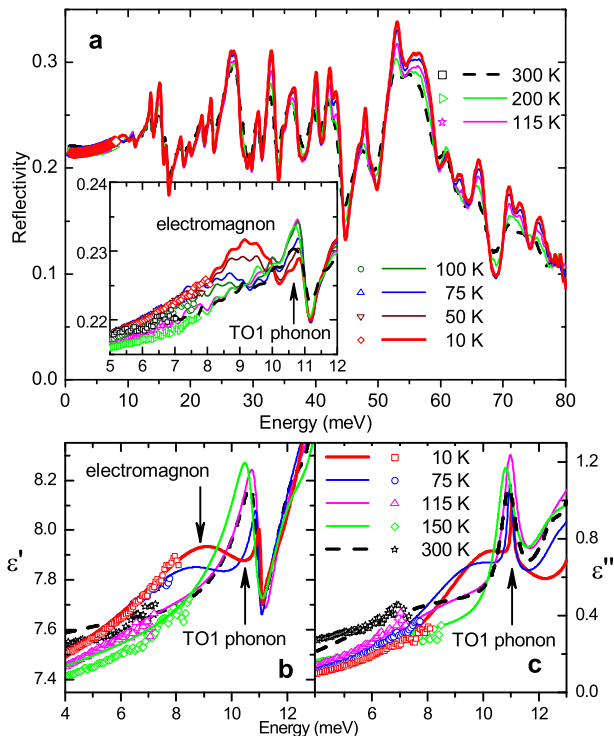


FIG. 1. (a) Lines: IR reflectivity spectra showing polar phonons. Symbols below 8 meV: data calculated from THz spectra. The inset shows in detail the low-energy part where, below 100 K and 10 meV, a new reflection band appears due to the EM. (b), (c): Fits of the complex permittivity in the far IR region, obtained from the IR reflectivity spectra using a sum of harmonic oscillators (lines), compared to data obtained from THz spectroscopy (symbols).

phonon (see Fig. 2), evidencing a coupling among these three polar modes. Despite the lattice distortions which occur between 150 K and 75 K, the crystal symmetry of $\varepsilon\text{-Fe}_2\text{O}_3$ does not change with temperature^{35,37}. This is further confirmed by our IR reflectivity spectra, displaying a temperature-independent number of polar phonons; should a structural phase transition occur, it would imply a change of the factor group analysis and different phonon selection rules. Given the high number of atoms in the unit cell, multiple new reflection bands throughout the IR range would be observed. Therefore, one can exclude the new mode to originate in a structural modification.

Another option to be considered is the polar phonon splitting due to exchange coupling below AFM phase transitions which was reported in various transition-metal monoxides and chromium spinels³⁸; the mode splitting increased on cooling below the Néel temperature. However, this explanation cannot be valid as we observe an opposite temperature dependence—the new mode appears below T_m at low energies and hardens towards the TO1 phonon energy on cooling, i.e. their energy difference decreases.

Finally, one cannot a priori exclude the hypothesis of

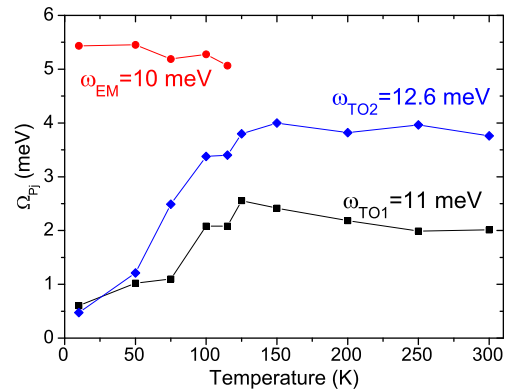


FIG. 2. Temperature dependence of the plasma frequencies (defined as $\Omega_{pj} = \sqrt{\Delta\varepsilon_j\omega_j}$) of the 10-meV-mode attributed to EM and of the TO1 and TO2 phonons. The dielectric strengths $\Delta\varepsilon_j$ were evaluated by fitting using a model with harmonic oscillators.

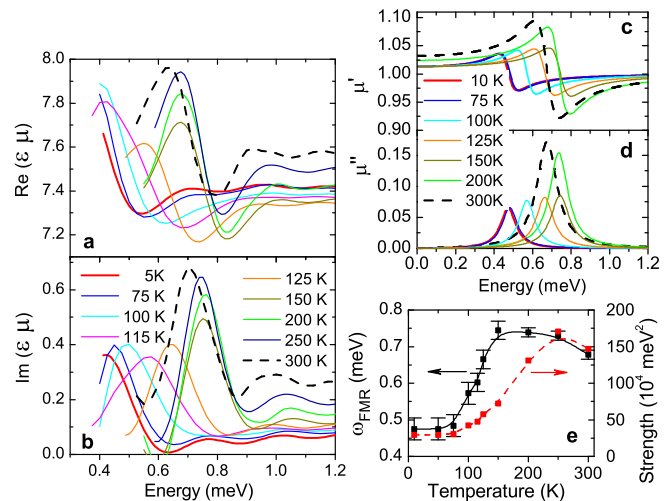


FIG. 3. Temperature dependence of the spectra of the (a) real and (b) imaginary parts of the $\varepsilon\mu$ product, obtained by THz spectroscopy. Spectra of μ' (c), μ'' (d), corresponding to the FMR mode, obtained by fitting the THz spectra. (e) Temperature dependence of the FMR energy and strength $\Delta\mu\omega_{\text{FMR}}^2$ derived from parts c, d.

activation of the TO1 phonon branch from the area of the BZ near its edge. This would require a folding of the structural BZ which could be caused by a transfer of the magnetic BZ folding (linked to incommensurability) via magnetostriction. Nevertheless, in the X-ray diffraction studies, no appropriate satellite reflections were observed. Even supposing these satellite reflections to be very weak, one would expect the off-center phonons to activate also at higher energies, which we did not observe. This hypothesis therefore seems unlikely. Based on further experimental evidence, especially in view of an analogous temperature behavior observed by INS, we argue below that the reflection band activated below T_m is most probably an EM.

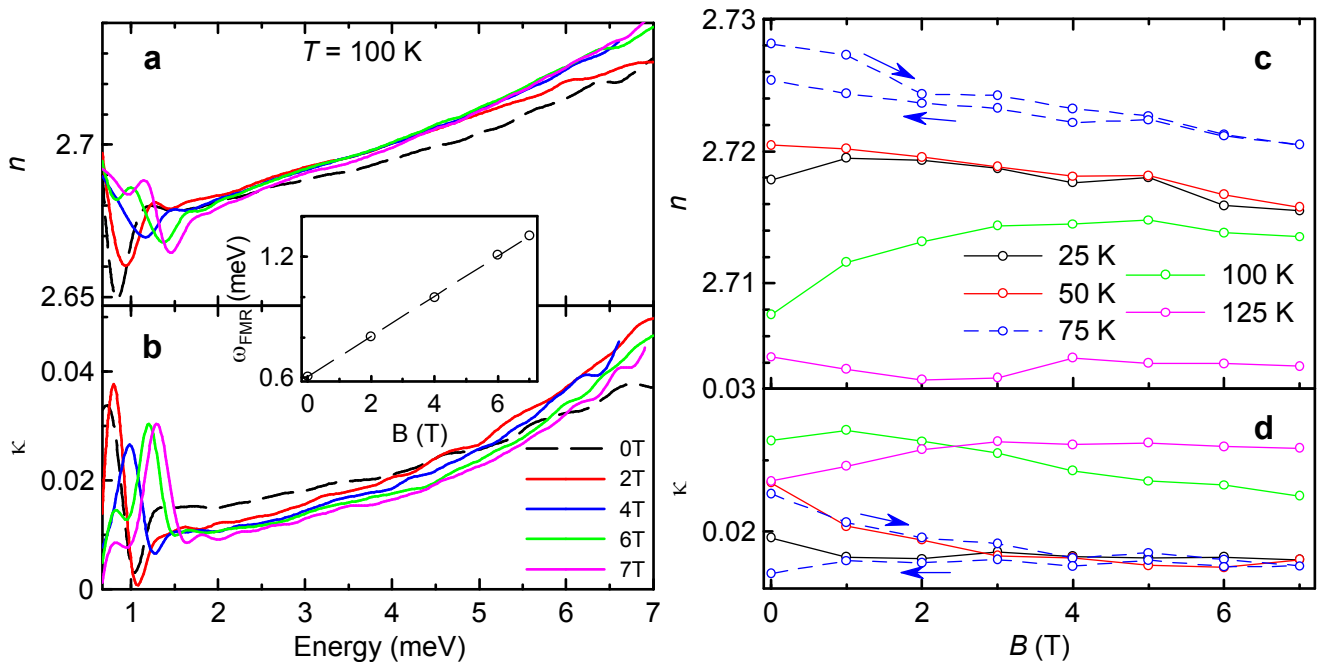


FIG. 4. (a), (b): Spectra of complex refractive index $N \equiv n - i\kappa$ of ε -Fe₂O₃ measured by THz spectroscopy at $T = 100$ K as a function of applied magnetic field. Inset: B -dependence of the FMR frequency, determined as the peak in $\kappa(E)$ spectra. (c), (d): Changes of the value of n , κ , determined within ± 0.001 , for $E = 5$ meV as a function of temperature and increasing magnetic field (except at 75 K).

The temperature dependent THz spectra (see Fig. 3) reveal the sharp FMR which was previously reported at room temperature^{25,26}. To quantify its temperature behavior, we used the harmonic oscillator model for all phonons and one term accounting for the FMR in $\mu(E)$, while assuming a smooth dependence of $\varepsilon(E)$ in this interval. The resulting spectra, matching well the measured data, are shown in Fig. 3c,d. From the fit parameters, we derived the temperature dependence of the magnon strength and FMR energy (see Fig. 3e). We observe a sharp drop in the resonance energy between 150 K and 75 K, very similar to that of the coercive field $H_c(T)$ ³⁹. This can be explained by the fact that the FMR energy is proportional to the magnetocrystalline anisotropy field H_a . As the sample consists of randomly oriented particles with a uniaxial magnetic anisotropy, H_a is proportional to the H_c value²⁷.

Furthermore, we measured THz time-domain spectra with external magnetic field ranging from 0 to 7 T. Because of the high absorption of the EM, lying near 10 meV, the sample was opaque above 7 meV. Therefore, we could measure only the low-frequency wing of the EM. When the magnetic field is applied, two types of changes in the THz spectra can be observed: an increase of the FMR frequency corresponding to the peak of the $\kappa(E)$ spectra, and a change of the slope of both real and imaginary parts of the index of refraction, indicating shifts of the EM frequency with magnetic field. An example of the former behavior at $T = 100$ K is shown in Fig. 4a, b; the FMR frequency, upon applying a static magnetic

field of $B = 7$ T, increases from 0.6 to 1.3 meV (see inset of Fig. 4a, b). The latter phenomenon is illustrated by Fig. 4c, d which traces the values of the complex refractive index at $E = 5$ meV as a function of temperature and applied magnetic field. While changes only close to the sensitivity level were detected at temperatures of 10 and 300 K (not shown in Fig. 4), there is a clear B -dependence of the spectra at intermediate temperatures. The highest sensitivity was observed at 100 K, close to the magnetic phase transition. Also, at $T = 75$ K, a marked hysteresis in B occurs, similarly to the temperature hysteresis observed by radio-frequency impedance spectroscopy techniques near this temperature (see Figure 5); this observation will be discussed below. At $T \ll T_m$, where the magnetic structure is probably stable, the changes of N with magnetic field are smaller. This explains also why we did not detect any significant changes of the far-IR spectra with magnetic field at $T = 2$ K.

In the frequency range from $f = 10$ Hz to 1 MHz, the complex permittivity ε was measured by impedance spectroscopy as a function of temperature (see Fig. 6). No sign of a FE phase transition was detected. Above 200 K, both $\varepsilon'(T)$ and $\varepsilon''(T)$ increase due to the leakage conductivity and the related Maxwell-Wagner polarization. Between 100 and 200 K, we observed a step-like decrease of $\varepsilon'(T)$ towards lower temperatures and maxima in losses $\tan \delta(T, f) = \varepsilon''(T, f)/\varepsilon'(T, f)$, which is typical of a dielectric relaxation. The temperature dependence of the relaxation time $\tau(T)$ obtained from the peaks of $\tan \delta(T, f)$ follows an Arrhenius behavior, $\tau(T) =$

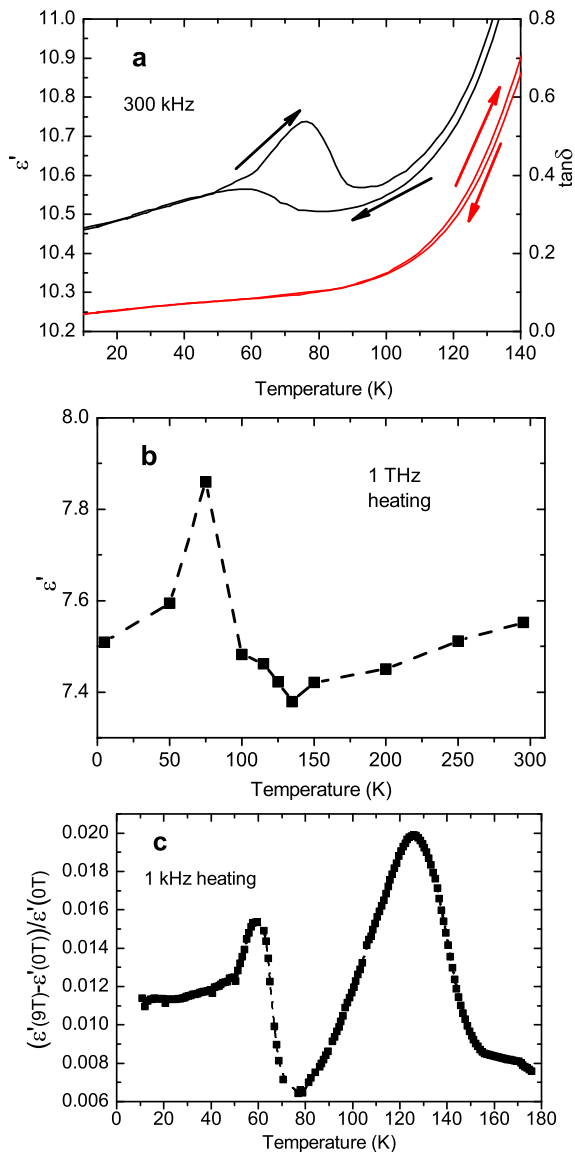


FIG. 5. (a) Temperature hysteresis of the dielectric permittivity (black lines, left axis) and losses (red lines, right axis) observed at 300 kHz. (b) Temperature dependence of the permittivity at 1 THz measured on heating. The dashed line is a guide to the eyes. The values at 300 kHz are systematically higher than at 1 THz due to a small dielectric relaxation between these two frequencies; one can see a similar permittivity peak near 75 K in both experiments. (c) Temperature dependence of relative changes of the 1 kHz-permittivity due to magnetic field with $B = 9$ T (taken on heating).

$\tau_0 e^{E_0/k_B T}$ with k_B denoting the Boltzmann constant, $\tau_0 = (1.5 \pm 0.2) \times 10^{-12}$ s and $E_0 = (0.195 \pm 0.002)$ eV. The origin of this relaxation is not clear, however, similar effects are known from several perovskite rare-earth manganites, including the multiferroics TbMnO_3 and DyMnO_3 ⁴⁰. We attribute the relaxation to thermally activated vibrations of the FE domain walls or magnetic domain walls which can be polar⁴¹. The huge room-

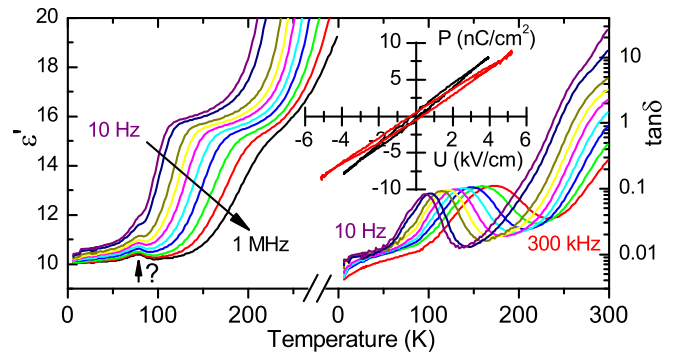


FIG. 6. Temperature dependence of the real permittivity ϵ' (left) and dielectric losses $\tan \delta$ (right), measured upon heating by impedance spectroscopy. Inset: dependence of the polarization on the applied 50 Hz ac bias at 120 K (black) and 15 K (red).

temperature coercive field H_c is the consequence of a single-domain magnetic structure of the nanograins²⁶. Below 200 K, H_c strongly decreases due to a transition to a polydomain structure³⁹ which explains why the dielectric relaxation exists only in this temperature range.

The inset of Fig. 6 shows the measured dependences of the polarization on applied electric field. No open FE hysteresis loops nor signs of saturation were observed under the applied fields. Since the $Pna2_1$ crystal structure of ϵ - Fe_2O_3 corresponds to a pyroelectric space group, we cannot exclude that an applied electric field with an intensity higher than the one we used (beyond 5 kV/cm, our sample became leaky) would switch the polarization and that ϵ - Fe_2O_3 is in fact FE. Actually, one of us recently investigated strained epitaxial ϵ - Fe_2O_3 thin films and, under an applied electric field one order of magnitude stronger, observed a room-temperature FE switching.⁴² Since the crystal symmetry of ϵ - Fe_2O_3 does not change with temperature⁴³, one can not exclude that the ϵ - Fe_2O_3 nanograins are also FE already above the ferromagnetic phase transition occurring near 490 K; in any case, it is at least pyroelectric. Consequently, ϵ - Fe_2O_3 would belong to type-I multiferroics.

Near 75 K, a small peak in $\epsilon'(T)$ was observed in our impedance spectroscopy measurements (as marked by the arrow in Fig. 6). This peak is rather weak on cooling, but it becomes more distinct on heating, and it exhibits a temperature hysteresis of ≈ 15 K (see also Fig. 5). This is reminiscent of a dielectric anomaly typical for pseudoproper or improper FE phase transitions, such as those in perovskite rare-earth manganites. However, this hypothesis is not confirmed by the polarization measurements shown in Fig. 6, and the X-ray and neutron diffraction investigations did not reveal any structural changes near 75 K either^{35,37}. In type-II multiferroics, a narrow dielectric peak is seen at T_c only at frequencies below 1 MHz and its intensity strongly decreases with rising frequency⁴⁰. By contrast, in our impedance spectra, the peak is present at all frequencies up to the THz re-

gion (see Fig. 5b), although it is partly covered by the stronger dielectric relaxation at low frequencies. Therefore, this anomaly must originate from phonons or an EM. As the observed dielectric anomaly occurs at a temperature close to the lowest-temperature magnetic phase transition³⁵, we propose that it arises from the transfer of the dielectric strength from the TO1 and TO2 phonons to the EM (see Fig. 2). We note that in single-crystal multiferroics, often a step-like increase of the permittivity occurs below the temperature where the electromagnon activates.¹³ Our observations on nanograin samples are somewhat different—while a step-like increase of ϵ' below ≈ 130 K, superimposed with the narrow-range anomaly near 75 K, was detected in the THz range (see Fig. 5b), only the anomaly near 75 K manifests itself in the kHz range (see Fig. 5a). We suppose that the step in the low-frequency permittivity is screened by the observed dielectric relaxation in the microwave range.

We also investigated the dependence of the permittivity at 1 kHz on external magnetic field up to 9 T. We found that $\epsilon'(B)$ exhibits the highest changes (almost 2%) near 70 and 130 K (see Fig. 5c). Both of these anomalies are clearly linked to the changes of magnetic structure³⁵. We suppose that the lower-temperature change corresponds to the EM anomaly observed also in THz experiments, while that observed near 130 K is due to the relaxation linked to the magnetic and simultaneously polar domain walls.

B. Neutron scattering.

In order to further explore the hypothesis of an EM, we performed time-of-flight INS experiments which allow measuring the phonon and magnon density of states (DOS) in the meV energy range. As the nanopowder does not allow us to determine directly the phonon and magnon dispersion branches in the BZ, the data represent an orientation-averaged scattering function $S(Q, E)$ where Q is the total momentum transfer and E the energy transferred between the crystal lattice and the neutrons (see Fig. 7). The data reveal a steep column of intense scattering, emanating from magnetic Bragg peaks at $Q = 1.4 \text{ \AA}^{-1}$, and extending up to $E \sim 10$ meV. The weaker columns at $Q > 2 \text{ \AA}^{-1}$ are due to scattering in higher-order BZs. The fact that the area of most intense scattering is located at low Q shows unambiguously⁴⁴ that the dominant contribution to the low- Q scattering comes from spin waves.

A qualitatively similar magnon response was recently observed in INS spectra of polycrystalline BiFeO_3 ⁴⁵; the spin wave character of the excitation was confirmed by INS on BiFeO_3 crystals, where the magnon dispersion branch was directly measured⁴⁶. Our scattering from the magnon waves becomes weaker on cooling due to the decreasing Bose-Einstein factor. Around 10 meV, a distinct scattering peak persists down to low temperatures, corresponding to a maximum of the magnon DOS; this

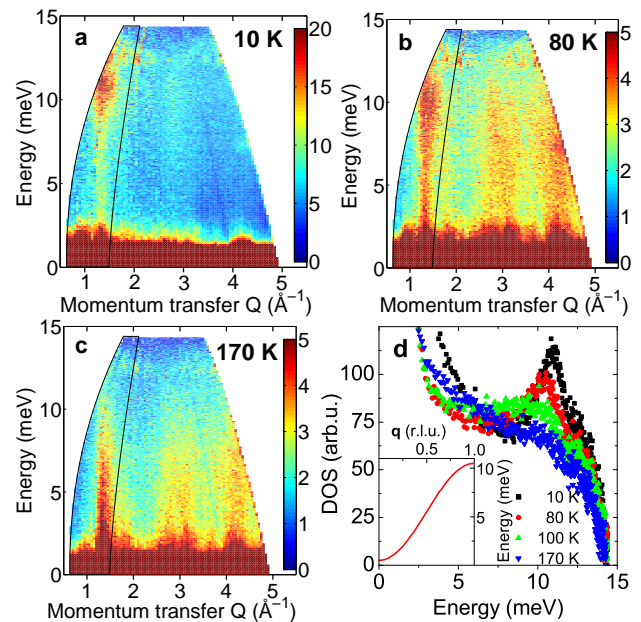


FIG. 7. (a), (b), (c): Bose-Einstein-factor-normalized INS intensity as a function of momentum Q and energy E transfers for $T = 10, 80$ and 170 K. Near $Q = 1.4 \text{ \AA}^{-1}$, a magnon branch with a cut-off energy of ≈ 11 meV can be seen. (d): DOS determined by integrating over the regions marked by black solid lines in (a)–(c). Inset of (d): scheme of the magnon dispersion branch in reciprocal lattice units, involving the FMR and EM near the BZ center and boundary, respectively.

is obviously due to a flat end of the branch below the BZ boundary. Moreover, the energy at the maximal magnon DOS, as well as its temperature evolution, corresponds to that of the newly IR-activated mode (see Fig. 7d).

The inset of Fig. 7d shows a schematic view of an acoustic-like magnon dispersion branch giving rise to the observed excitations, both the one below 10.5 meV (at the BZ boundary) and the FMR near 0.5 meV (in the BZ center). This dispersion behavior is similar to that observed in the ferrimagnetic HoFe_2 ⁴⁷, which exhibits a slightly higher Curie temperature of 597 K. In $\epsilon\text{-Fe}_2\text{O}_3$, the optic-like magnon branches lie probably above 12 meV, beyond the energy range used in our INS experiments. We suggest that this acoustic-like magnon is activated in the IR spectra due to the loss of magnetic translation symmetry in the incommensurate magnetic phase below T_m . Such an activation is analogous to that of phonons with $q \neq 0$ in structurally modulated crystals⁴⁸. We suppose that the large damping of the newly activated excitation can be explained by an activation of the magnon DOS in the IR spectra. Since the observed spin-wave excitation is coupled with the lowest-energy TO1 phonon, it must be excited by the electric component of the electromagnetic radiation; at the same time, it has to contribute to dielectric permittivity. Therefore, the excitation seen near 10 meV must be an EM.

IV. CONCLUSION

In conclusion, in $\varepsilon\text{-Fe}_2\text{O}_3$, we have discovered an excitation, appearing simultaneously with the modulation of the magnetic structure, at energies below the TO1 phonon. We attribute this excitation to an EM whose energy corresponds to a magnon from the BZ boundary. We did not observe any other excitation at lower energies, in contrast to type-II multiferroics. There, the Dzyaloshinskii-Moriya (D.-M.) interaction breaks the center of symmetry, induces ferroelectricity¹¹ and the EMs are activated thanks to magnetostriction ($(\mathbf{S}_i \cdot \mathbf{S}_j)$ -type interaction)⁷. In $\varepsilon\text{-Fe}_2\text{O}_3$, the crystal structure is acentric at all temperatures and it permits to activate the D.-M. interaction in an originally collinear ferrimagnetic structure⁴⁹; the D.-M. interaction tilts the spins and finally induces an incommensurately modulated magnetic structure below $T_m = 110$ K, where the EM activates due to magnetostriction.

Up to now, EMs were reported mainly in type-II multiferroics. Previous reports of EMs in type-I multiferroics were lacking evidence of their coupling with polar phonons, e.g. in BiFeO_3 ¹⁹⁻²¹ or hex-YMnO_3 ²². Our results indicate that $\varepsilon\text{-Fe}_2\text{O}_3$ belongs to type-I multiferroics; it is pyroelectric and perhaps FE even above the ferrimagnetic phase transition⁴³ at 490 K, but the EM is activated only below T_m , corresponding to the onset of the incommensurately modulated magnetic structure. In our case, a clear transfer of dielectric strength from a low-energy phonon to the zone boundary magnon was observed.

Finally, we would like to stress that EMs were previously identified only in single crystals using a thorough polarization analysis of measured spectra. Here we have determined an EM from unpolarized IR and THz spectra of nanograin ceramics showing its coupling with a TO1 phonon. Simultaneously, we have shown from INS experiments made on powder that the EM in $\varepsilon\text{-Fe}_2\text{O}_3$ comes from the BZ boundary. This combination of experimental methods provides a guideline for an unambiguous determination of EMs in materials where sufficiently large single crystals for polarized IR and THz measurements are not available.

ACKNOWLEDGMENTS

This work was supported by the Czech Science Foundation (project P204/12/1163). The experiment in ILL Grenoble was carried out at the IN4 spectrometer within the project LG11024 financed by the Ministry of Education of the Czech Republic. M.G. acknowledges funding from the Spanish Ministerio de Economía y

Competitividad (projects RyC-2009-04335, MAT 2012-35324 and CONSOLIDER-Nanoselect-CSD2007-00041) and the European Commission (FP7-Marie Curie Actions, PCIG09-GA-2011-294168). S.K. thanks Petr Brázda for his stimulation of our $\varepsilon\text{-Fe}_2\text{O}_3$ research and S. Artyukhin for a helpful discussion.

Appendix A: Phonons in $\varepsilon\text{-Fe}_2\text{O}_3$

For the orthorhombic $Pna2_1$ crystal structure of $\varepsilon\text{-Fe}_2\text{O}_3$ with 8 formula units per unit cell³⁵, the factor group analysis predicts the following phonon counts and symmetries in the BZ center:

$$\Gamma = 30A_1(z, x^2, y^2, z^2) + 30A_2(xy) + 30B_1(x, xz) + 30B_2(y, yz). \quad (\text{A1})$$

Here, x , y and z mark electric polarizations of the IR wave for which the phonons are IR active, while the rest of symbols are components of the Raman tensor. After subtraction of the three acoustic phonons, 87 IR-active phonons are expected. We have observed 35 of them (see their parameters in Table I); the remaining ones cannot be identified, either because of low intensities or because they overlap with other ones.

No.	$\Delta\varepsilon$	Ω_0 [meV]	Γ [meV]	No.	$\Delta\varepsilon$	Ω_0 [meV]	Γ [meV]
EM	0.27	10.47	4.67	18	0.02	38.40	1.34
1	0.01	11.05	0.13	19	0.18	40.13	1.40
2	0.01	12.61	0.87	20	0.15	42.16	1.37
3	0.08	13.85	0.44	21	0.13	43.37	1.48
4	0.24	15.25	0.82	22	0.02	46.76	0.99
5	0.06	16.26	0.49	23	0.16	48.04	1.87
6	0.02	17.58	1.82	24	0.02	49.39	1.20
7	0.07	18.64	0.83	25	0.25	52.78	2.24
8	0.03	19.95	0.76	26	0.40	55.42	4.68
9	0.09	21.87	0.99	27	0.07	57.45	3.03
10	0.08	23.42	0.65	28	0.11	60.84	3.32
11	0.56	27.18	2.33	29	0.03	63.02	1.95
12	0.02	28.88	0.77	30	0.14	65.66	3.62
13	0.01	29.59	0.46	31	0.07	70.78	2.29
14	0.09	30.91	0.96	32	0.03	72.58	1.96
15	0.21	33.05	1.12	33	0.07	75.29	3.61
16	0.01	34.94	0.44	34	0.05	78.46	4.71
17	0.37	36.44	2.60	35	0.08	85.68	5.43

TABLE I. Set of parameters used in the oscillator model to fit the IR reflectance data at 10 K. $\Delta\varepsilon$, Ω_0 and Γ mark the dielectric contribution, eigenfrequency and damping of polar modes. The first row contains the parameters of the electromagnon, the other rows describe 35 polar phonons. From mid-IR reflectivity, the high-frequency electronic contribution was obtained as $\varepsilon_\infty = 3.2$.

- * Corresponding author; e-mail: kadlec@fzu.cz
- ¹ J. Scott, Nat. Mater. **6**, 256 (2007).
 - ² A. Roy, R. Gupta, and A. Garg, Adv. in Cond. Matt. Phys. **2012**, 926290 (2012).
 - ³ V. V. Kruglyak, S. O. Demokritov, and D. Grundler, J. Phys. D: Appl. Physics **43**, 264001 (2010).
 - ⁴ C. Nan, M. Bichurin, S. Dong, D. Viehland, and G. Srinivasan, J. Appl. Phys. **103**, 031101 (2008).
 - ⁵ A. Pimenov, A. Mukhin, V. Ivanov, V. Travkin, A. Balbashov, and A. Loidl, Nat. Phys. **2**, 97 (2006).
 - ⁶ R. Valdés Aguilar, A. B. Sushkov, C. L. Zhang, Y. J. Choi, S.-W. Cheong, and H. D. Drew, Phys. Rev. B **76**, 060404 (2007).
 - ⁷ R. Valdés Aguilar, M. Mostovoy, A. B. Sushkov, C. L. Zhang, Y. J. Choi, S.-W. Cheong, and H. D. Drew, Phys. Rev. Lett. **102**, 047203 (2009).
 - ⁸ Y. Takahashi, R. Shimano, Y. Kaneko, H. Murakawa, and Y. Tokura, Nat. Phys. **8**, 121 (2012).
 - ⁹ M. P. V. Stenberg and R. de Sousa, Phys. Rev. B **85**, 104412 (2012), *ibid.* **80**, 094419 (2009).
 - ¹⁰ M. Mochizuki, N. Furukawa, and N. Nagaosa, Phys. Rev. Lett. **104**, 177206 (2010).
 - ¹¹ D. Khomskii, Phys. **2**, 1 (2009).
 - ¹² A. Sushkov, R. Aguilar, S. Park, S. Cheong, and H. Drew, Phys. Rev. Lett. **98**, 27202 (2007).
 - ¹³ A. B. Sushkov, M. Mostovoy, R. V. Aguilar, S.-W. Cheong, and H. D. Drew, J. Phys.: Cond. Matt. **20**, 434210 (2008).
 - ¹⁴ A. Pimenov, A. M. Shuvaev, A. A. Mukhin, and A. Loidl, J. Phys.: Cond. Matt. **20**, 434209 (2008).
 - ¹⁵ N. Kida, Y. Takahashi, J. Lee, R. Shimano, Y. Yamasaki, Y. Kaneko, S. Miyahara, N. Furukawa, T. Arima, and Y. Tokura, J. Opt. Soc. Am. B **26**, A35 (2009).
 - ¹⁶ S. Seki, N. Kida, S. Kumakura, R. Shimano, and Y. Tokura, Phys. Rev. Lett. **105**, 097207 (2010).
 - ¹⁷ I. Kézsmárki, N. Kida, H. Murakawa, S. Bordács, Y. Onose, and Y. Tokura, Phys. Rev. Lett. **106**, 57403 (2011).
 - ¹⁸ A. M. Shuvaev, A. A. Mukhin, and A. Pimenov, J. Phys.: Cond. Matt. **23**, 113201 (2011).
 - ¹⁹ M. Cazayous, Y. Gallais, A. Sacuto, R. De Sousa, D. Lebeugle, and D. Colson, Phys. Rev. Lett. **101**, 37601 (2008).
 - ²⁰ D. Talbayev, S. Trugman, S. Lee, H. Yi, S. Cheong, and A. Taylor, Phys. Rev. B **83**, 094403 (2011).
 - ²¹ G. Komandin, V. Torgashev, A. Volkov, O. Porodinkov, I. Spektor, and A. Bush, Phys. Solid State **52**, 734 (2010).
 - ²² S. Pailhès, X. Fabréges, L. P. Régnault, L. Pinsard-Godart, I. Mirebeau, F. Moussa, M. Hennion, and S. Petit, Phys. Rev. B **79**, 134409 (2009).
 - ²³ C. Kadlec, V. Goian, K. Z. Rushchanskii, P. Kužel, M. Ležaić, K. Kohn, R. V. Pisarev, and S. Kamba, Phys. Rev. B **84**, 174120 (2011).
 - ²⁴ L. Machala, J. Tuček, and R. Zbořil, Chem. Mater. **23**, 3255 (2011).
 - ²⁵ A. Namai, S. Sakurai, M. Nakajima, T. Suemoto, K. Matsumoto, M. Goto, S. Sasaki, and S. Ohkoshi, J. Am. Chem. Soc. **131**, 1170 (2008).
 - ²⁶ A. Namai, M. Yoshikiyo, K. Yamada, S. Sakurai, T. Goto, T. Yoshida, T. Miyazaki, M. Nakajima, T. Suemoto, and H. Tokoro, Nat. Commun. **3**, 1035 (2012).
 - ²⁷ S. Ohkoshi, S. Kuroki, S. Sakurai, K. Matsumoto, K. Sato, and S. Sasaki, Angew. Chem. Int. Ed. **46**, 8392 (2007).
 - ²⁸ J. Tuček, R. Zbořil, A. Namai, and S. Ohkoshi, Chem. Mater. **22**, 6483 (2010).
 - ²⁹ M. Gich, J. Gazquez, A. Roig, A. Crespi, J. Fontcuberta, J. C. Idrobo, S. J. Pennycook, M. Varela, V. Skumryev, and M. Varela, Appl. Phys. Lett. **96**, 112508 (2010).
 - ³⁰ Y. Ding, J. Morber, R. Snyder, and Z. Wang, Adv. Funct. Mater. **17**, 1172 (2007).
 - ³¹ J. Jin, S. Ohkoshi, and K. Hashimoto, Adv. Mater. **16**, 48 (2004).
 - ³² S. Sakurai, J. Jin, K. Hashimoto, and S. Ohkoshi, J. Phys. Soc. Japan **74**, 1946 (2005).
 - ³³ J. Tuček, S. Ohkoshi, and R. Zbořil, Appl. Phys. Lett. **99**, 253108 (2011).
 - ³⁴ E. Tronc, C. Chanéac, and J. Jolivet, Journal of Solid State Chemistry **139**, 93 (1998).
 - ³⁵ M. Gich, C. Frontera, A. Roig, E. Taboada, E. Molins, H. R. Rechenberg, J. D. Ardisson, W. A. A. Macedo, C. Ritter, V. Hardy, et al., Chem. Mater. **18**, 3889 (2006).
 - ³⁶ M. Gich, C. Frontera, A. Roig, J. Fontcuberta, E. Molins, N. Bellido, C. Simon, and C. Fleta, Nanotechnology **17**, 687 (2006).
 - ³⁷ Y.-C. Tseng, N. M. Souza-Neto, D. Haskel, M. Gich, C. Frontera, A. Roig, M. van Veenendaal, and J. Nogués, Phys. Rev. B **79**, 094404 (2009).
 - ³⁸ C. Kant, M. Schmidt, Z. Wang, F. Mayr, V. Tsurkan, J. Deisenhofer, and A. Loidl, Phys. Rev. Lett. **108**, 177203 (2012).
 - ³⁹ M. Gich, A. Roig, C. Frontera, E. Molins, J. Sort, M. Popovici, G. Chouteau, D. M. y Marero, and J. Nogués, J. Appl. Phys. **98**, 044307 (2005).
 - ⁴⁰ F. Schrettle, P. Lunkenheimer, J. Hemberger, V. Y. Ivanov, A. A. Mukhin, A. M. Balbashov, and A. Loidl, Phys. Rev. Lett. **102**, 207208 (2009).
 - ⁴¹ A. Pyatakov, D. Sechin, A. Sergeev, A. Nikolaev, E. Nikolaeva, A. Logginov, and A. Zvezdin, Europhys. Lett. **93**, 17001 (2011).
 - ⁴² M. Gich, I. Fina, A. Morelli, F. Sánchez, M. Alexe, J. Fontcuberta, and A. Roig (in preparation).
 - ⁴³ D. Nižňanský, private communication. (No change of the Pna_21 crystal structure was observed in XRD up to 800 K).
 - ⁴⁴ G. Shirane, S. M. Shapiro, and J. M. Tranquada, *Neutron Scattering with a Triple-Axis Spectrometer* (Cambridge University Press, 2002), pp. 36 ff.
 - ⁴⁵ O. Delaire, M. B. Stone, J. Ma, A. Huq, D. Gout, C. Brown, K. F. Wang, and Z. F. Ren, Phys. Rev. B **85**, 064405 (2012).
 - ⁴⁶ J. Jeong, E. A. Goremychkin, T. Guidi, K. Nakajima, G. S. Jeon, S.-A. Kim, S. Furukawa, Y. B. Kim, S. Lee, V. Kiryukhin, et al., Phys. Rev. Lett. **108**, 077202 (2012).
 - ⁴⁷ J. J. Rhyne and N. C. Koon, J. Appl. Phys. **49**, 2133 (1978).
 - ⁴⁸ J. Petzelt, Phase Trans. **2**, 155 (1981).
 - ⁴⁹ C. Fennie, Phys. Rev. Lett. **100**, 167203 (2008).